

OBSCURING FRACTION OF ACTIVE GALACTIC NUCLEI: IMPLICATIONS FROM RADIATION-DRIVEN FOUNTAIN MODELS

KEIICHI WADA

Kagoshima University, Kagoshima 890-0065, Japan

Draft version May 11, 2019

ABSTRACT

Active galactic nuclei (AGNs) are believed to be obscured by an optical thick “torus” that covers a large fraction of solid angles for the nuclei. However, the physical origin of the tori and the differences in the tori among AGNs are not clear. In a previous paper based on three-dimensional radiation-hydrodynamic calculations, we proposed a physics-based mechanism for the obscuration, called “radiation-driven fountains,” in which the circulation of the gas driven by central radiation naturally forms a thick disk that partially obscures the nuclear emission. Here, we expand this mechanism and conduct a series of simulations to explore how obscuration depends on the properties of AGNs. We found that the obscuring fraction f_{obs} for a given column density toward the AGNs changes depending on both the AGN luminosity and the black hole mass. In particular, f_{obs} for $N_H \geq 10^{22} \text{ cm}^{-2}$ increases from ~ 0.2 to ~ 0.6 as a function of the X-ray luminosity L_X in the $L_X = 10^{42-44} \text{ ergs s}^{-1}$ range, but f_{obs} becomes small (~ 0.4) above a luminosity ($\sim 10^{45} \text{ ergs s}^{-1}$). The behaviors of f_{obs} can be understood by a simple analytic model and provide insight into the redshift evolution of the obscuration. The simulations also show that for a given L_{AGN} , f_{obs} is always smaller ($\sim 0.2 - 0.3$) for a larger column density ($N_H \geq 10^{23} \text{ cm}^{-2}$). We also found cases that more than 70% of the solid angles can be covered by the fountain flows.

Subject headings: galaxies: active – galaxies: nuclei – ISM: structure – X-rays: galaxies – method: numerical

1. INTRODUCTION

Active galactic nuclei (AGNs) such as quasars and Seyfert galaxies are important objects in the cosmic history. The enormous radiation energy of AGNs significantly influences the formation and evolution of galaxies and their environment. The evolution of AGNs in high redshift has been studied by wide-field optical and X-ray surveys, and these studies have recently become statistically more reliable based on large samples (e.g., Ueda et al. 2014; Pâris et al. 2014; Buchner et al. 2015; Aird et al. 2015). However, because AGNs are believed to be surrounded by an optically thick material for a fraction of the solid angles, we do not necessarily observe all the radiation from the nuclei. Because this obscuration may affect the apparent evolution of the luminosity function (Merloni & Heinz 2013), the fraction of absorbed objects is an essential quantity not only for interpreting observations (e.g., Lawrence & Elvis 1982; La Franca et al. 2005; Ballantyne et al. 2006; Hasinger 2008; Han et al. 2012) but also for theoretical models of AGNs evolution (e.g., Enoki et al. 2003; Fanidakis et al. 2011; Enoki et al. 2014).

The fraction of obscured objects, hereafter called the obscured fraction f_{obs} , can be estimated by various observational methods. The nature of the obscuration should be different depending on the wavelength, central luminosity, and redshift, suggesting a complicated nature and evolution of the environment around AGNs (e.g., Lawrence & Elvis 2010; Merloni et al. 2014). In particular, f_{obs} inferred from optical and infrared observations is relatively high ($f_{obs} \sim 0.4 - 0.6$) (Roseboom et al. 2013; Lusso et al. 2013; Shao et al. 2013) and shows weak dependence on the luminosity, whereas X-ray samples suggest that f_{obs} decreases with increasing X-ray luminosity (Ueda et al. 2003; Hasinger 2008; Han et al. 2012; Merloni et al. 2014; Ueda et al. 2014). This case may be understood using the receding torus model (Lawrence 1991; Simpson 2005), but recent surveys with large samples (*XMM-Newton* and *Swift-BAT*) suggested more complicated behavior in terms of L_X : f_{obs} is small for both low and high luminosities (i.e., there is a peak for a certain luminosity). The redshift evolution of f_{obs} is also suggested by different groups, although the results are not fully consistent each other (Burlon et al. 2011; Brightman & Nandra 2011; Ueda et al. 2014; Buchner et al. 2015; Aird et al. 2015).

The obscuring fraction as a function of the AGN luminosity and observed wavelength should be related to the morphology, internal structures, and size of the torus. If the obscured fraction of AGNs are related to the luminosity of AGNs, it would be natural to assume that such obscuring properties are directly caused by the radiative and mechanical feedback from the AGNs. As discussed by Elvis (2012), the weak correlation between the X-ray and optical obscuration might suggest that obscuration is occurred on different scales. The optical property of the X-ray-selected AGNs suggest that the radiation environment around the nucleus may determine the properties of the obscuration (Merloni et al. 2014).

The obscuration is not necessarily caused by static structures of the interstellar medium (ISM), such as the “donut-like” torus (Urry & Padovani 1995). Recently, Wada (2012) showed that radiation from the accretion disk drives

vertical circulation of gas flows on the order of a few to tens of parsecs, forming thick torus-like structures. Based on this model, type-1 and -2 SEDs can be also consistently explained as a result of the outflows and backflows (Schartmann et al. 2014). This “radiation-driven fountain” has an advantage that it naturally explains a long-standing question about the torus paradigm: how does the torus maintain its thickness? At a much smaller scale, the outflows originating in the accretion disk could obscure the nucleus (Elvis 2000; Proga et al. 2000; Nomura et al. 2013). Moreover, Elitzur (2006) also claimed that the doughnut-like torus is not necessary, based on a similar picture.

In this paper, using three-dimensional radiation-hydrodynamic simulations, which are based on Wada (2012) and Schartmann et al. (2014), we investigate how the obscured fraction depends on the properties of AGNs, i.e., luminosity and black hole mass (or Eddington ratio). In §2, the numerical methods and models are described, and the numerical results are shown in §3. The results are analytically discussed using a simple toy model in §4. The origin of the obscuring fraction suggested by recent surveys are discussed in §5, and the summary and remarks for the present study are given in §6. Here, we focus on the effect of the radiative feedback from the AGNs alone; possible synergetic effects with nuclear starbursts (e.g., Wada et al. 2002) will be discussed elsewhere.

2. NUMERICAL METHODS AND MODELS

2.1. Numerical methods

We follow the same numerical methods in this study as those presented in Paper I: three-dimensional hydrodynamic equations are solved by an Eulerian hydrodynamic code with a uniform grid, accounting for radiative feedback processes from the central source using a ray-tracing method. The methods are briefly summarized here.

Based on our three-dimensional, multi-phase hydrodynamic model (Wada et al. 2009), we included the radiative feedback from the central source, i.e., the radiation pressure on the surrounding gas and the X-ray heating. In contrast to previous analytical and numerical studies of radiation-dominated tori (e.g., Pier & Krolik 1993; Shi & Krolik 2008; Dorodnitsyn et al. 2011), we assume neither dynamical equilibrium nor geometrical symmetry. Outflows are naturally expected under the AGN feedback as also explored by Dorodnitsyn et al. (2012), in which infrared dominated flows in a pc-scale torus, by using time-dependent, axisymmetric radiation hydrodynamic simulations with a flux-limited diffusion.

We further account for the self-gravity of the gas, radiative cooling, uniform ultraviolet (UV) radiation for photoelectric heating, and H_2 formation/destruction. However, to clarify only the effects of the radiation feedback, we do not include the effect of supernova feedback in this study.

The hydrodynamic part of the basic equations is solved using the advection upstream splitting method (AUSM) (Liou & Steffen 1993) and its improved scheme AUSM⁺ (Liou 1996). We use 128^3 grid points for the hydrodynamics calculations. The uniform Cartesian grid covers a 32^3 pc³ region around the galactic center with a spatial resolution of 0.25 pc. The Poisson equation is solved to calculate the self-gravity of the gas using the fast Fourier transform, and the convolution method uses 256^3 grid points.

The radiation source is an accretion disk whose size is five orders of magnitude smaller than the grid size in the present calculations. Therefore, we assumed that the radiation is emitted from a point source. However, the radiation flux originating from the accretion disk is assumed to be non-spherical (see §2.2). The optical depth τ_ν is calculated at every time step along a ray from the central source at each grid point; 128^3 rays are used in the computational box. We assume a cooling function based on a radiative transfer model of photodissociation regions (Meijerink & Spaans 2005) for $20 \text{ K} < T_{\text{gas}} < 10^8 \text{ K}$, which is a function of the molecular gas fraction f_{H_2} and the far ultraviolet (FUV) intensity G_0 (Wada et al. 2009). Here, we assume solar metallicity and $G_0 = 1000$. The main radiative heating source for the ISM is the X-ray, which reflect interactions between high-energy secondary electrons and thermal electrons (Coulomb heating) as well as H_2 ionizing heating in the warm and cold gases (Maloney, Hollenbach, & Tielens 1996; Meijerink & Spaans 2005).

The temperature of the interstellar dust T_{dust} at a given position irradiated by the central source is calculated by assuming thermal equilibrium (e.g., Nenkova et al. 2008). If $T_{\text{dust}} > 1500 \text{ K}$, we assume that the dust is sublimate. Here, we assume that the ISM in the central several tens parsecs is optically thin with respect to the re-emission from the host dust. The SED of the AGN and the dust absorption cross-section are taken from Laor & Draine (1993). We use a standard galactic dust model, which is the same as that used by Schartmann et al. (2010).

2.2. Initial conditions and model parameters

We follow the three-dimensional evolution of a rotating gas disk in a fixed spherical gravitational potential under the influence of radiation from the central source. To prepare quasi-steady initial conditions without radiative feedback, we first run models of axisymmetric and rotationally supported thin disks with uniform density profile. After the thin disks are dynamically settled, the radiation feedback is turned on.

Free parameters in the present simulations is the luminosity of the AGN (L_{AGN}) and the black hole mass (M_{BH}). The Eddington ratios L_{AGN}/L_E , for the Eddington luminosity $L_E \equiv 4\pi G c m_p M_{\text{BH}}/\sigma_T$, are changed from 0.01 to 0.5 for three black hole masses: $M_{\text{BH},8} \equiv M_{\text{BH}}/10^8 M_\odot = 0.13, 1.3$, and 13. The total AGN luminosity ranges $1.6 \times 10^{43} - 8.0 \times 10^{46} \text{ erg s}^{-1}$, which correspond to X-ray luminosities of $L_{X,44} \equiv L_X/(10^{44} \text{ ergs s}^{-1}) = 0.01 - 8.35$. We also prepare the initial gas disk with two different densities: $\rho_0 = 1.2$ and $3.6 \times 10^3 M_\odot \text{ pc}^{-3}$. Thus, the gas mass fraction to the black hole mass ranges from 4×10^{-4} to 0.12. The AGN luminosity is assumed to be constant during calculations, which is typically a few million years.

We have modified some assumptions in Paper I to achieve more realistic models. As is in Paper I, the accretion disk itself is not solved in present simulations, and we assume an anisotropic radiation field for the central source. In contrast to the assumption in Paper I, i.e. $F_{AGN} \propto \cos \theta$ for all wavelength, here the ultraviolet flux changes as $F_{UV}(\theta) \propto \cos \theta(1 + 2 \cos \theta)$ (Netzer 1987), where θ denotes the angle from the rotational axis (z -axis) in order to take into account the limb darkening effect of the thin accretion disk. As a result, the UV flux is about 20% larger for the z -axis and 25% smaller at $\theta \sim 60^\circ$ than the case in Paper I. Since the X-ray radiation would be originated in the hot coronal atmosphere of the accretion disk (Netzer 1987; Xu 2015), here we simply take spherical symmetry for the X-ray flux. In Paper I, L_X was fixed to 10% of the bolometric luminosity, but here we use luminosity-dependent correction for the X-rays (Hopkins et al. 2007) (2–10 keV) and for the B -band (Marconi et al. 2004). The X-ray luminosity for $M_{BH} = 1.3 \times 10^7 M_\odot$ is about half of that assumed in paper I. In paper I, we also simply assumed that the hypothetical accretion disk is parallel to the galactic disk. However, in reality, any orientations of the accretion disk could be possible in dependent of the galactic disk (e.g. Kawaguchi & Mori 2010). Here we assumed that the direction of the emerging non-spherical radiation is inclined by 45° from the rotational axis of the circumnuclear gas disk in some models, and its three-dimensional gas dynamics is fully followed without assuming any symmetry.

The dust-to-gas ratio is assumed to be a widely used value, i.e. 0.01, instead of 1/30 in Paper I, although the actual ratio is not clear in the AGN environment.

As summarized in Table 1, we explored a total of 24 different sets of parameters (each model name represent parameters as described in the caption).

3. NUMERICAL RESULTS: OBSCURATION BY RADIATION-DRIVEN FOUNTAIN

In this section, we derive the obscuring fraction for a given column density toward the nucleus using a quasi-steady three-dimensional density distribution under the influence of the radiation feedback. The results are summarized as a function of the X-ray luminosity.

Four representative models of the density structures of the gas at a quasi-stable state are shown in Fig. 1. Figure 1a shows a typical radiation-driven fountain of the gas (Paper I), which consists of bipolar, non-steady, non-uniform outflows, failed winds (back flows to the disk), and a dense, thin disk. Physical origin of the fountain flows was partly discussed in paper I, but here we add some analysis of the numerical results in Appendix A-1. See also the simple model in §4 for conditions to generate outflows. As discussed in Appendix A-1.2, the system reaches to a quasi-steady state of the gas circulation after about 2 rotational period at $r = 10$ pc, which is $t \sim 0.5$ Myr for $M_{BH} = 1.3 \times 10^3 M_\odot$.

Using the density distribution, the column density toward the nucleus as a function of the viewing angles (θ_v) and the azimuthal angles is plotted in Fig. 2a. In Fig. 2, column densities for the models shown in Fig. 1 are also plotted. Among these models, the column density tends to increase toward $\theta_v = 0$ (edge-on) and reaches the maximum of $N_H \geq 10^{25} \text{ cm}^{-2}$. This occurs because of the stable existence of the dense, thin gas disk for which the radiation from the central source does not affect the disk except for the central part. The bipolar outflows and the failed winds cover a fraction of solid angles for the central source in model 8D50 (Fig. 1a). Therefore, the nucleus is obscured for $|\theta_v| \lesssim 90^\circ$ and $|\theta_v| \lesssim 20^\circ$ for $N_{22} \equiv 10^{22} \text{ cm}^{-2}$ and $N_{23} = 10N_{22}$, respectively. The density change for the azimuthal direction causes 0.5–1.0 dex difference in the column density for a given viewing angle, which causes a small ambiguity for the obscured fraction (f_{obs}) as a function of the column density.

Figure 3 shows radial distribution of the cumulative column densities in a typical fountain model (8D50), from which we can know where the obscuration mostly occurs for a given line-of-sight. It shows that $N_H \gtrsim 10^{22} \text{ cm}^{-2}$ at $r = 16$ pc (i.e. the edge of the computational box) is mostly attained the gas inside 5–10 pc, whose structures are resolved by 20–40 numerical grid points.

In some low luminosity models (e.g., model 7L01: $L_{X,44} = 0.011$ and $M_{BH,8} = 0.13$) no steady outflows are observed (Fig. 1b), and as a result, the opening angle of the obscuring material becomes large with $f_{obs}(N_{22}) \equiv f_{obs,22} = 0.33$ (Fig. 2b). On the other hand, the obscuring fraction also becomes small ($f_{obs,22} \simeq 0.4$) for high luminosity with a massive black hole (model 9L40: $L_{X,44} = 7.08$ and $M_{BH,8} = 13$), such as those shown in Fig. 1c and 2c. These high luminosity models do not also show steady bipolar outflows. This is because the acceleration due to the radiation pressure for dusty gas is not sufficiently large to reach the escape velocity for the luminous models, in which the dust sublimation radius moves outward ($\propto L_{AGN}^{1/2}$). This is discussed using a kinematic model in §4.

As a result of the fully three-dimensional calculations, the central radiation source (the accretion disk) is not restricted to a parallel configuration with the rotational axis of the gas disk. In reality, the accretion disk should not necessarily be in the same plane of the circumnuclear gas disk. We found that if the axis of the central source is inclined by 45° from the rotational axis of the disk, and the Eddington ratio is relatively high ($\gtrsim 0.3$), the majority of the solid angle for the AGN is covered by the fountain gas (Fig. 1d and 2d).

The obscuring fraction of all 24 models are summarized in Table 1 and Fig. 4, where f_{obs} for N_{22} and N_{23} are plotted for each model as a function of $L_{X,44}$. Figure 4 shows that nature of the obscuration depends on the luminosity of AGNs, and $f_{obs,22}$ is small in both low and high luminosity cases. Moreover, $f_{obs,22}$ shows a maximum value of 0.8–0.9 around $L_{X,44} \sim 0.2 - 1.0$. The obscuring fraction for N_{23} gradually increases from $f_{obs,23} \simeq 0.1$ to 0.3 in a range of $L_{X,44} = 0.01 - 10$, which is almost the same as the initial conditions. This reflects that the scale height of the dense part of the disk is larger for more luminous models (i.e., more massive black holes). For a less dense column density, $f_{obs,22}$ increases from 0.3 to 0.5–0.6 toward $L_{X,44} \sim 1.0$, as a consequence of the formation of radiation-driven fountains. There is no significant difference on f_{obs} between models with different initial gas density ρ_0 .

We also find that $f_{obs,22}$ becomes quite large ($\sim 0.7 - 0.9$) for parameters that cause outflows ($\gamma_{edd} \gtrsim 0.3$ and $M_{BH,8} = 0.13$ or 1.3) when the central accretion disk is inclined by 45° (Fig. 1d, 2d, and open blue symbols in Fig. 4). This occurs because the gas circulation between the outflows and the dense gas effectively covers a large fraction of the solid angle. On the other hand, for more luminous AGNs ($L_{X,44} > 2$), the outflows are stalled; therefore, a relatively small obscured fraction is observed. For a given parameter set, note that f_{obs} should have an ambiguity of $\sim 10\%$, which comes from the azimuthal inhomogeneous structures of the fountains (see Fig. 2).

Although the overall structures of N_H presented here is similar to those found in paper I, there are some differences, because of the modified assumptions (§2.2). The radiative feedback assumed in this paper is less effective for generating outflows than those in paper I for the same BH mass. Moreover the present models show smaller dispersion of N_H for a given viewing angle θ , especially for smaller θ . This is partly because the circumnuclear disks in the present model keep its geometrically thin shape in the computational box. On the other hand, the disks are followed by twice larger computational box in paper I (i.e. 64^3 pc). The disks tend to be gravitational unstable in the outer part (see discussion in Appendix A-1.2), where gravity of the BH is weaker, resulting in geometrically thick, inhomogeneous disk. This thick disks are not uniform for the azimuthal direction (see for example Fig. 7 in paper I), therefore the column density for a given viewing angle show dispersion. Although most obscuration is occurred in the central 10 pc, distributions and structures in the outer part of the disk on several tens parsecs scale may contribute to the observed column density, especially for the viewing angles close to the edge-on. Therefore, N_H could have larger dispersions, and as a result the obscuring fraction especially for $N \gtrsim 10^{23} \text{ cm}^{-2}$ presented here might be a “lower” limit with the contribution of the attenuation by the gas on larger scales.

4. A SIMPLE ANALYTIC MODEL

As shown in §3 and paper I, the three-dimensional gas dynamics under the effect of the non-spherical radiation are generally complicated. However, a simple kinematic model is helpful for understanding the behavior of the radiative feedback and the origin of the dependence of f_{obs} on L_{AGN} in Fig. 4.

In the phenomena discussed here, the primary driving force producing the fountain of gas around the AGNs is the radiation pressure for the dusty gas. We assume that the accretion disk radiates most of its energy toward the direction of the rotational axis, not toward the plane of the gas disk (except for the case of the inclined accretion disk). On the other hand, the radiative heating more isotropically affects the surrounding gas through advection. The X-ray radiation from the AGN, which is assumed to be spherically symmetric in this study, heats the inner part of the thin gas disk, making it geometrically thick. Thus, we expect that the gas is radially accelerated by the radiation pressure with assistance from the X-ray heating. In the following discussion, the effect of the gaseous pressure in the outflowing gas and the self-gravity of the gas are ignored for simplicity. The outflowing gas is also dealt as a “parcel” or “shell”, that is the attenuation of the central radiation by the outflows themselves are ignored.

Let us first assume that the X-ray heating causes the inner part of the gas disk to be a quasi-stable, uniform sphere with radius r_0 , as schematically shown in Fig. 5. In the gas sphere with $r = r_0$, the radiative cooling with cooling rate Λ_{cool} is assumed to be balanced with the X-ray heating rate: $\rho_g^2 \Lambda_{cool} \sim L_X / (4\pi r_0^3 / 3)$, where ρ_g is the average gas density. Then, the radius r_0 within which the X-ray heating is effective is

$$r_0 \sim (3L_X / 4\pi \rho_g^2 \Lambda_{cool})^{1/3}. \quad (1)$$

Now, let us assume that the gas at $r > r_d$ is accelerated due to the radiation pressure of the dust, where r_d is the dust sublimation radius¹. Therefore, for the velocity v_0 at $r = r_0$, energy conservation requires

$$\frac{1}{2} (v_0^2 - v_{max}^2) = GM_{BH} \left(\frac{1}{r_0} - \frac{1}{r_{max}} \right), \quad (2)$$

where r_{max} is the maximum radius that the launched gas reaches at maximum velocity v_{max} . For the dusty gas with opacity κ and dust-to-gas ratio γ_d , the gas can be accelerated toward v_{max} due to radiation pressure from r_0 to r_{max} :

$$v_{max}^2 \sim \frac{\kappa \gamma_d L_{AGN}(\theta)}{4\pi c} \left(\frac{1}{r_0} - \frac{1}{r_{max}} \right), \quad (3)$$

where $L_{AGN}(\theta)$ is the non-spherical radiation field of the AGN depending on the angle from the rotational axis θ . Similarly, v_0 is the velocity attained by to the radiation pressure from r_d to r_0 , i.e.,

$$v_0^2 \sim \frac{\kappa \gamma_d L_{AGN}(\theta)}{4\pi c} \left(\frac{1}{r_d} - \frac{1}{r_0} \right). \quad (4)$$

Using eq. (2), (3), and (4), we obtain r_{max} as a function of L_{AGN} and M_{BH} :

$$r_{max}(L_{AGN}, M_{BH}) = \frac{\hat{L}_{AGN} + GM_{BH}}{GM_{BH}/r_0 - \hat{L}_{AGN}(1/r_d - 2/r_0)}, \quad (5)$$

¹ In the following discussion, we assume that $r_0 > r_d$, which is always the case for $L_{AGN} < 10^{47} \text{ erg s}^{-3}$ with the parameter chosen here.

where $\hat{L}_{AGN} \equiv \kappa\gamma_d L_{AGN}/(8\pi c)$. If $r_{max} \rightarrow \infty$, the velocity of the dusty gas becomes larger than the escape velocity, and we expect that an outflow is formed.

For simplicity, we take $L_{AGN}(\theta) = 1/2 L_{UV} |\cos(\theta)|$, rather than $L_{AGN}(\theta) \propto \cos\theta(1 + 2\cos\theta)$ as in the numerical simulations, where L_{UV} is the UV luminosity of the AGN. This difference is not essential for the following discussion. If $GM_{BH}/r_0 = \hat{L}_{AGN}(1/r_d - 2/r_0)$ in eq. (5), then r_{max} tends toward infinity for the critical angle θ_{crit} , which is derived as

$$\cos\theta_{crit} = \frac{GM_{BH}}{r_0} \frac{16\pi c}{\kappa\gamma_d L_{UV}} \left(\frac{1}{r_d} - \frac{2}{r_0} \right)^{-1} \quad (6)$$

$$= \frac{\sigma_T}{m_p \kappa \gamma_d \gamma_{Edd} r_0} \left(\frac{1}{r_d} - \frac{2}{r_0} \right)^{-1}, \quad (7)$$

where γ_{Edd} is the Eddington ratio, σ_T is the Thomson cross-section, and m_p is the proton mass. We expect that, for $\theta < \theta_{crit}$, the radiation force is sufficiently large to allow the dusty gas to escape. Thus, we expect that, for this cone region, outflows of gas are formed. Otherwise, the gas launched from the inner region can only reach $r = r_{max}(\theta)$. We suppose that this gas eventually falls back toward the equatorial plane, which corresponds to the backflows seen in the hydrodynamic simulations (Fig. 1a and Wada (2012)).

Since both the equilibrium radius r_0 (eq. (1)) and the dust sublimation radius r_d depend on the luminosity of the AGN (e.g., $r_d \propto L_{AGN}^{0.5}$), r_{max} and θ_{crit} cannot simply be functions of the Eddington ratio γ_{Edd} , but they depend on both the AGN luminosity and the black hole mass. For non-spherical radiation, r_{max} is also a function of the angle θ . In Fig. 6, we plot $r_{max}(\theta)$ for five different parameter sets of $L_{46} \equiv 10^{46} \text{ ergs s}^{-1}$ and $M_{BH,8} \equiv 10^8 M_\odot$, showing the maximum radius of the launched gas. Here, we assume that $r_d = 1.3 L_{46}^{1/2} \text{ pc}$ (e.g., Lawrence 1991) and $\Lambda_{cool} = 10^{-22}/n_H^2 \text{ erg cm}^3 \text{ s}^{-2}$. For $(L_{46}, M_{BH,8}) = (0.02, 0.1)$ and $(0.2, 1.0)$ (red and blue lines), $r_{max}(\theta)$ has finite values for some angles; thus, conical outflows are expected for $\theta < \theta_{crit}$. In the remaining three models with $(L_{46}, M_{BH,8}) = (2.0, 10.0)$, $(10.0, 10.0)$, and $(0.01, 1.0)$, the accelerated gas cannot escape at any angle. In these cases, we suspect that steady outflows are not formed or they are stalled.

In Fig. 7, we plot θ_{crit} (eq. (7)) as a function of M_{BH} and $L_{X,44}$. Constant Eddington ratios are also shown with dotted lines. Here, we assume $\kappa = 10^3 \text{ cm}^2 \text{ g}^{-1}$ and $\rho_g = 300 M_\odot \text{ pc}^{-3}$. We also use the bolometric correction for X-rays (Hopkins et al. 2007) and for the B-band (Marconi et al. 2004). Figure 7 shows that there are regions where no outflows are formed, i.e., θ_{crit} has no value. For a given black hole (BH) mass ($M_{BH} \lesssim 10^9 M_\odot$), there is a lower limit of the luminosity forming the outflows (i.e., $\pi/2 > \theta_{crit} > 0$), under which the radiation pressure for the dusty gas is not sufficiently large to make the outflow velocity larger than the escape velocity. Interestingly, there is also an upper limit of the luminosity forming the outflows. This limit occurs because the dust sublimation radius r_d becomes close to the cooling radius r_0 ; as a result, the factor $(1/r_d - 2/r_0)^{-1}$ is dominant in eq. (7).

As we found in the radiation-driven fountain in the radiation-hydrodynamic simulations in Paper I and §2, part of the bipolar outflows driven by radiation from the AGNs falls back to the disk plane, forming a thick disk (the torus). The opening angle of the outflow can then be simply assumed to be close to the critical angle θ_{crit} derived in the above argument. Thus, for larger θ_{crit} , the obscuration fraction f_{obs} is expected to be smaller. On the other hand, if r_{max} is not infinity for all of the angles, the outflow is not formed. In this case, we expect that the central source is visible for most viewing angles².

Based on these simple arguments, we can qualitatively understand the numerical results in §3. We found that the obscuration fraction for a given column density, especially for N_{22} , increases with the luminosity of the AGN, and turns to be a small value above $L_X \gtrsim 10^{45} \text{ erg s}^{-1}$. The increase of obscuration is consistent with the behavior of the opening angle as a function of the central luminosity (Fig. 7). If the BH is too massive, e.g., $M_{BH} > 10^9 M_\odot$, however the outflow is not expected even for large luminosity. This situation occurs in the numerical simulations, and as a result, we observe a relatively small obscuration fraction for high luminosity AGNs.

In the simplest version of the receding torus model (Lawrence 1991; Hasinger 2008), a constant scale height is assumed for the gas disk. Then, the dust sublimation radius, which is a function of the central luminosity, is the only factor affecting the opening angle. However, our radiation hydrodynamics calculations and analytic argument provide a more dynamic picture. The radiation from the AGNs naturally drives outflows if conditions are satisfied, which affect the obscuring nature. The response of the dust to the central radiation is important, but this response would be more dynamically related with the obscuration than that assumed in the static receding torus model.

Note, however, that strong outflows are observed in some luminous quasars, which could originate in the line-driven wind from the accretion disk (Elvis 2000; Proga et al. 2000; Nomura et al. 2013). The line-driven outflows also contribute to the obscuration and could be related with ultra-fast outflows (UFOs).

5. IMPLICATIONS TO OBSERVATIONS

5.1. Torus structures inferred from f_{obs}

In the simplest picture of the torus paradigm, the tori for all AGNs have the same geometry, and the observed fraction of type-1 and 2 AGNs can be used to infer the opening angle of the torus. However, there is increasing evidence that the obscuring material around the nucleus depends on the properties of the AGNs.

² The hydrodynamic simulations actually show more complicate dynamics of the gas for marginal cases, that is the gas shells are launched and falling back showing intermittent behavior.

The covering fraction of AGNs due to the surrounding gas can be estimated by the fraction of the reprocessed infrared radiation to the bolometric luminosity of AGN (Maiolino et al. 2007; Treister et al. 2008; Lusso et al. 2013), or from the fraction of type-2 AGNs based on X-ray spectroscopy (Ueda et al. 2003; Hasinger 2008). However, there is discrepancy in the fraction among the observational results. The obscuring fraction inferred from optical and infrared observations is relatively high ($f_{obs} \sim 0.4 - 0.6$) (Lawrence & Elvis 2010; Roseboom et al. 2013) and shows weak dependence on the luminosity of AGNs, whereas X-ray samples suggest that f_{obs} decreases (from ~ 0.8 to ~ 0.1) with increasing luminosity in the $L_X = 10^{42-46} \text{ erg s}^{-1}$ range (Lawrence et al. 2013). Based on 513 type-1 AGNs in the *XMM-COSMOS* survey, Lusso et al. (2013) show that the obscuring fraction ranges between $f_{obs} = 0.75 - 0.45$ or $0.45 - 0.30$, depending on the assumed physical properties of the torus, especially on its optical thickness³. The optically thick case seems consistent with the receding torus model (Simpson 2005), but the scale height of the torus is required to weakly increase as a function of the bolometric luminosity to fit the observed results. Based on *WISE-UKIDSS-SDSS* data, Roseboom et al. (2013) found that the ratio L_{IR}/L_{bol} , which should be related to the covering factor (CF), shows a log-normal distribution around $CF \sim 0.3 - 0.4$ for luminous quasars. This might represent the variety in the obscuring material structures.

Recently, based on the analysis of AGNs at $z < 0.2$ from *SDSS DR7*, Oh et al. (2015) suggested that the type-1 AGN fraction depends on both the black hole mass and bolometric luminosity, shaping a “ridge” where the fraction of type-1 AGNs is low (< 0.2) on the plane of $L_{bol} - M_{BH}$ (see Fig. 16 in Oh et al. (2015)). For a given M_{BH} , the obscured fraction is larger for less luminous, sub-Eddington AGNs. These results are roughly consistent with the analysis in §4 and Fig. 7.

These observations and our results presented here suggest that the obscuration of the AGNs should be a much more complicated phenomenon than the standard picture based on a static, dusty torus or a disk (see also a recent review by Netzer 2015). The discrepancy between X-rays and longer wavelength radiation in terms of f_{obs} implies that multiple components of the ISM contribute the obscuration on various scales. Our numerical simulations showed that radiative feedback causes non-steady, non-uniform structures of the multi-phase gas around the nucleus, and these structures are affected by at least the luminosity of AGNs and the black hole mass. We should note, however that this situation could be even more complicated because many AGNs are associated with nuclear starbursts (e.g. Esquej et al. 2014), which could also contribute to the obscuration (Wada et al. 2002).

5.2. Origin of luminosity-dependent obscuration in X-rays

We now focus on the X-ray properties of the obscuration. Recent X-ray spectral surveys based on large samples have reported that the fraction of the obscured objects changes depending on the AGN luminosity. In other words, f_{obs} rapidly decreases as the luminosity increases (Hasinger 2008; Ueda et al. 2003; Burlon et al. 2011; Brightman & Nandra 2011; Ueda et al. 2014; Merloni & Heinz 2013; Aird et al. 2015); the absorbed AGNs are less than $\sim 30\%$ for luminous AGNs at $L_X \sim 10^{45} \text{ erg s}^{-1}$, whereas the fraction of the absorbed AGNs is more than 70% for less luminous ones at $\sim 10^{43} \text{ erg s}^{-1}$. Several studies have also claimed that the fraction of obscured AGNs *increases* with L_X (Burlon et al. 2011; Brightman & Nandra 2011; Buchner et al. 2015) for lower luminosities. These results suggest that the fraction of the obscured AGNs in low redshift objects peaks ($f_{obs} \sim 0.70 - 0.8$) around $L_X \sim 10^{42.5-43} \text{ erg s}^{-1}$.

The behavior of f_{obs} in terms of the X-ray luminosity is basically consistent with the results shown in §3, even though we found that AGNs with $L_X \sim 10^{43-44} \text{ erg s}^{-1}$ are the most effectively obscured, which is one order of magnitude larger than those suggested by observations. Interestingly, this behavior rather fits high redshift ($z > 1.5 - 2.1$ in Buchner et al. (2015)) objects (see §5.3).

Buchner et al. (2015) schematically illustrated how the obscured fraction depends on the luminosity (see Fig. 13 in Buchner et al. (2015)). In particular, they suggested that at low luminosities, *torus clouds are produced by the disk wind* (e.g., Elitzur & Shlosman 2006), and a *receding torus caused by cloud ionization* (e.g., Lawrence 1991) is proposed for the reason of the declining obscuring fraction for luminous objects. These pictures are partly similar to results we have shown here, but the outflows are not actually caused by the disk wind, which is a much smaller scale phenomenon (see, for example Proga et al. (2000); Nomura et al. (2013)) than that considered here. In our radiation-hydrodynamic models, dusty gas irradiated by the central radiation source and its attenuation are implemented in the circumnuclear region. However, in contrast to the original receding torus model, the response of the dusty gas is much more dynamic. Davies et al. (2015) analyzed 20 AGNs observed by *Swift/BAT* as well as results by Merloni et al. (2014), which is based on 1310 AGNs observed *XMM-COSMOS* survey. They found that optical and X-ray properties of the absorption are different depending on the luminosity. They proposed a modified version of the receding torus with a *neutral* torus inside the dusty molecular torus by which the X-rays are absorbed. In our simulations, the strong radiation from the accretion disk causes the dust-free region inside the dense dusty gas, and this also affects generation of the outflows.

Buchner et al. (2015) also suggested that Compton-thick AGNs occupy about half of the the number and luminosity densities of the obscured population. The fraction of Compton-thick AGNs to the total population is constant ($\sim 35\%$) and is independent of the redshift and accretion luminosity. In our numerical models, f_{obs} for a larger column density (i.e., N_{23}) slightly increases from $\sim 15\%$ to 20% over the luminosity range of $L_X = 10^{42-45} \text{ erg s}^{-1}$, and there is no peak around $L_X \sim 10^{44} \text{ erg s}^{-1}$, which contrasts the behavior of f_{obs} for N_{22} . This occurs because the obscuring

³ Note that the SED-based obscuring fraction does not necessarily represent the true value. For example, Schartmann et al. (2014) derived f_{obs} directly from the optical depth calculated from the numerical results of the radiation-driven fountain model (Wada 2012). They compare their results with f_{obs} derived using a similar method by Lusso et al. (2013) (see (Lusso et al. 2013) and their Fig. 12) and found that the SED-based f_{obs} (0.7) is effectively smaller than the directly determined value (0.9).

structures around AGNs basically consist of three components: a geometrically thin cold disk, a thick warm disk, and non-steady bipolar outflows (Schartmann et al. 2014). The Compton-thick obscuration is mainly caused by dense, thin disks. As a natural consequence, there are fewer chances to observe nuclei with higher column densities (see Fig. 11 and 12 in Buchner et al. (2015)). Jia et al. (2013) claimed that the column density obtained from X-ray absorption is nearly constant ($\sim 10^{22.9} \text{ cm}^{-2}$) in 71 type-2 quasars. Our results suggest that $f_{\text{obs}}(N_{23})$ is 20–30% for the most luminous models with $L_{\text{bol}} > 10^{46} \text{ erg s}^{-1}$. The circumnuclear gas disks in these models are similar without showing strong outflows, suggesting that we have fewer chances to observe luminous quasars with a *mild* obscuration with small column density (e.g., $< 10^{22} \text{ cm}^{-2}$).

5.3. Implication to the origin of the redshift evolution

The X-ray surveys discussed in the previous section also showed that obscured AGNs (Compton-thin AGNs) increase toward $z = 3 - 5$. For example, Buchner et al. (2015) showed that the fraction of the absorbed AGNs is ~ 0.7 and ~ 0.6 at $L_{X,44} \simeq 1$ and 10, respectively, at $z=3$ in contrast to $\sim 0.4 - 0.5$ at $z = 0.5$. Aird et al. (2015) also suggested similar results and claimed that $f_{\text{obs}}(L_X)$ differs depending on the luminosity at high- z . These studies also suggested that the fraction of Compton-thick objects is nearly constant (~ 0.4 or 0.2) toward $z = 3 - 5$.

Figure 8 shows the opening angle of the bipolar outflows derived from the same analytical model as that shown in Fig. 7. In this plot, θ_{crit} is plotted for three initial densities of the gas disk, i.e., $\rho_3 = 1.0, 5.0$, and 10, commonly showing that the opening angle becomes small as the central luminosity increases. Moreover, Fig. 8 shows that, for a given luminosity, θ_{crit} is smaller for denser gas, i.e., more obscured. If the gas density in the central region is not *too dense* (otherwise, there is no solution for θ_{crit} , meaning that outflows are not formed), AGNs could be *more obscured for more gas-rich environments*. If high- z AGNs are associated with denser gas compared to local objects, this result is qualitatively consistent with the trend shown by the X-ray survey. Note again that this result is suggested only by the framework of the radiative feedback. In reality, we suspect that, in very gas-rich objects at high- z , nuclear starbursts should be initiated, which could be also play a role in the obscuration through supernova feedback (e.g. Levenson, Weaver, & Heckman 2001; Wada et al. 2002).

6. SUMMARY AND REMARKS

Based on the radiation-driven fountain scenario (Wada 2012; Schartmann et al. 2014), which is the circulation of gas driven by the central radiation obscuring the nucleus, we investigated how the AGN properties, i.e., luminosity and black hole mass, affect the obscuration due to the circumnuclear ISM, using fully three-dimensional radiation-hydrodynamic simulations. The obscuring fraction f_{obs} is derived from distribution of column density N_{H} toward the nucleus, using the numerical simulations.

We found that f_{obs} changes depending on N_{H} , the total luminosity of the AGN (L_{AGN}), and the black hole mass (M_{BH}) (§3 and Fig. 6). For a given L_{AGN} , f_{obs} is always smaller ($\sim 0.2 - 0.3$) for large column density ($N_{\text{H}} > 10^{23} \text{ cm}^{-2}$) than that for a smaller column density $N_{\text{H}} > 10^{22} \text{ cm}^{-2}$. This is a natural consequence of the fact that the dense gas surrounding the nuclei is mostly concentrated on a thin disk.

We found that f_{obs} for $N_{\text{H}} = 10^{22} \text{ cm}^{-2}$ increases from ~ 0.2 to ~ 0.6 with the X-ray luminosity L_X in a range of $L_X = 10^{42-44} \text{ ergs s}^{-1}$, and f_{obs} becomes small ~ 0.4 at high luminosity ($\geq 2 \times 10^{44} \text{ ergs s}^{-1}$). At a moderate luminosity $L_X \sim 10^{44} \text{ ergs s}^{-1}$, a large fraction of the solid angles ($f_{\text{obs}} > 0.5$) can be obscured by the column density of $N_{\text{H}} \geq 10^{22} \text{ cm}^{-2}$, because of the outflows and thick disk caused by the back flows. The f_{obs} behavior has been simply demonstrated using a kinematic model (§4), in which the bipolar outflows are formed in specific ranges of L_{AGN} and M_{BH} (Fig.5 and Fig. 6), and their opening angles do not simply depend on the Eddington ratio.

The AGNs can be buried with $f_{\text{obs}} > 0.7$ for $N_{\text{H}} \geq 10^{22} \text{ cm}^{-2}$, when the central accretion disk is *inclined* by 45° from the rotational axis of the circumnuclear gas disk (Fig. 1d and 2d, and open symbols in Fig. 3). Even in this configuration, the radiative feedback from the accretion disk cannot destroy a dense gas disk from a few to tens of parsecs. This causes non-spherical circulations of the gas (Fig. 1d), and as a result, the majority of the solid angles are obscured by the gas with $N_{\text{H}} \leq 10^{22} \text{ cm}^{-2}$. The mass accretion can be possible through the dense gas disk, which is not completely destroyed, even in this case. This behavior could be a possible structure of “buried” AGNs.

The behavior of f_{obs} as a function of the X-ray luminosity is consistent with recent X-ray surveys (Burlon et al. 2011; Buchner et al. 2015; Aird et al. 2015) (§5.2). However, the luminosity for which f_{obs} reaches its maximum is a factor of ten smaller (i.e., $\sim 10^{43} \text{ erg s}^{-1}$) than the observations for local AGNs, and the luminosity would more accurately fit those suggested in AGNs at $z = 2 - 3$ (§5.3).

Note that we did not consider the effect of stellar feedback around AGNs in the present simulations and analysis. Many AGNs are associated with circumnuclear starbursts (e.g., Esquej et al. 2014; Netzer 2015), and high-velocity outflows of molecular and ionized gas are often observed in quasars and ultra-luminous infrared galaxies (ULIRGs). These activities could also change the structure of the circumnuclear disk, and as a result the obscuration of AGNs can be affected.

The author is grateful to R. Davies, M. Schartmann, Y. Ueda and N. Kawakatsu for many helpful comments and discussions. The author also appreciates many valuable comments and suggestions by the anonymous referee. The numerical computations presented in this paper were performed on a Cray XC30 at the National Astronomical Observatory of Japan.

A-1. APPENDIX

A-1.1. *Mechanism of the Outflows*

In this complementary section, we discuss dynamics and physical origin of the "radiation-driven fountain". One may notice in some models that vertical (z -direction) motions of the gas are driven (Fig. 1). Since the radiation pressure on the dusty gas due to the central radiation source is solved only for the radial direction by the ray-tracing method in this paper, this is mainly due to the effect of the gas pressure gradient caused by the radiative and mechanical heating and also by the density gradient. In Fig. 9, we show snapshots of density, temperature (T_g), Mach number (\mathcal{M}) for vertical direction (i.e. $\mathcal{M} \equiv v_z/c_s$, where c_s is the sound speed), and pressure distributions on the $x-z$ plane of model 8D50 (the inclination of the central accretion disk is zero). It shows that velocity of the gas in the bipolar outflows along the rotational axis (z -axis) is largest. This is natural because the flux due to the central source is largest for the direction. However, the directions of the outflows are not perfectly radial, especially near the central "core" (torus-like structure seen in the density map inside $r \sim 5$ pc) and the edges of the conical outflows. As seen in the temperature map (Fig. 9b), a hot core with $T_g \sim 10^7$ K is formed, which is directly heated by the X-ray from the central source. Its size roughly corresponds to the Compton radius $r_c \equiv GM_{BH}m_p/kT_g \simeq 4 \text{ pc} (T_g/10^7 \text{ K})^{-1} (M_{BH}/1.3 \times 10^8 M_\odot)$. In general, thermally driven wind is expected where $r > r_c$ (e.g. Begelman et al. 1983; Woods et al. 1996). This suggests that the gas motion just outside the hot core would be affected by the pressure gradient. However, as shown in Fig. 9c and 9d, the gases in the conical outflows are low temperature and highly supersonic ($\mathcal{M} > 10 - 20$) at least for the vertical direction. This implies that the thermal pressure cannot keep driving the outflow motion, and the radiation pressure plays a key role as discussed in section 4. This is an essential difference between the outflows observed here and the thermally driven "disk wind" from the accretion disk, which is a much smaller scale phenomenon and they are launched from the disk surface (Woods et al. 1996). The temperature of the gas disk in the present models are too low to generate the disk winds.

It is also interesting that the "back flows" are generated outside the cone, whose direction is not necessarily radial. For example, the accreting gases change their direction near the disk plane, which is due to the thermal pressure as suggested by the small Mach number and also due to the relatively small radiation pressure near the disk plane. Self-gravity of the gas disk may also contribute to disturb the radial flows.

A-1.2. *Quasi-stability of the System and Mass accretion to the Central BH*

Although the outflows driven by the radiation pressure is locally non-uniform and non-steady, we assume in §3 and §5 that the obscured nature is based on globally quasi-steady structures of the circumnuclear gas over ~ 1 Myr. Figure 10 shows the gas mass in the outflows ($|z| > 5$ pc) and the central core region ($r < 5$ pc). It shows that the outflows are formed in the first ~ 0.4 Myr, and a quasi-steady state is kept over 1 Myr. The gas mass in the central region is slightly decreasing with a rate of $\sim 0.2 M_\odot \text{ yr}^{-1}$, which is mostly caused by the outflows (see also discussion below). The total gas mass in the system is about $6 \times 10^6 M_\odot$, therefore the "life time" of the system would be $\sim 3 \times 10^7$ yr, if there is no mass supply from outside of the system.

Figure 11 shows time evolution of the gas mass just outside the inner boundary ($r \leq 0.75$ pc) of model 8D50 and 8D30i. It is significantly fluctuating (the time step is 50 years), and the distribution of the mass change rate dM_g/dt is roughly Gaussian as shown in the histogram. The root mean square (RMS) of dM_g/dt is $\sim 0.3 M_\odot \text{ yr}^{-1}$. Therefore if the short-period fluctuation of the gas mass caused by a temporal mass accretion toward the black hole and immediate by supply from the disk, the RMS accretion rate corresponds to about 10% Eddington accretion rate, which is comparable to the assumed luminosity of the central source. However, the average accretion rate over a longer period is much smaller; for example, for the "accretion phase" around $t = 1$ Myr (Fig. 11), the accretion rate is about $2 \times 10^{-3} M_\odot \text{ yr}^{-1}$. Therefore, the present simulations suggest that the radiation-driven fountain, whose time scale is at least $\sim \text{Myr}$, cannot be sustained only by the mass accretion through the disk on a sub-pc scale.

The mass accretion rate could be enhanced if the angular momentum transfer in the disk is more effective. This could be possible if the turbulent viscosity or gravitational torque due to the non-axisymmetric structures are enhanced due to gravitational instability (see for example Wada, Meurer, & Norman 2002, and references therein). The Toomre's Q value, $Q \equiv \kappa c_s / \pi G \Sigma_g$, where κ is epicyclic frequency and Σ_g is the surface density of the gas disk, is

$$Q \simeq 0.5 \left(\frac{c_s}{1 \text{ km s}^{-1}} \right) \left(\frac{\Sigma_g}{1000 M_\odot \text{ pc}^{-2}} \right)^{-1} \left(\frac{M_{BH}}{1.3 \times 10^7 M_\odot} \right)^{1/2} \left(\frac{r}{10 \text{ pc}} \right)^{-3/2}.$$

Therefore the disk around $M_{BH} = 1.3 \times 10^7 M_\odot$ can be gravitationally unstable even for most regions, if the temperature of the gas is smaller than 100 K. The gas temperature inside $r \lesssim 5$ pc is much larger than 10^4 K due to the X-ray heating, which is assumed to be spherical, thus disk becomes stable and geometrically thick (see Fig. 9a and 9b). On the other hand, outer disk ($r > 10$ pc) is expected to be gravitationally unstable especially for smaller BHs. The most unstable wavelength in the differentially rotating disk, $\lambda_J \equiv 2c_s^2/G\Sigma_g \simeq 1 \text{ pc} (T_g/100 \text{ K})(\Sigma_g/1000 M_\odot)^{-1}$, therefore the current spatial resolution, 0.25 pc, is marginal to resolve the gravitational instability of the coldest, thin gas disk (see also Fig. 12). However, the "effective" sound velocity including the velocity dispersion of the self-gravitationally unstable disk can be much larger than 1 km s^{-1} (see for example, Wada 2001; Wada, Meurer, & Norman 2002), and also by perturbation due to the back flows. As a result, the outer disk cannot be very thin (see Fig. 9) and the current spatial resolution is fine enough to resolve its vertical structures.

In order to clarify how the spatial resolution affects the mass accretion toward the center through gravitational instability, we run two additional test calculations, as shown by Fig.12. Since the radiation pressure does almost no effect on the gas disk itself due to the angle dependence of the radiation field and to save computational time, here we follow initial evolution of the disk without the radiation feedback. We take a vertically smaller computational box, i.e. $32^2 \times 8$ pc, which is solved using $128^2 \times 32$ or $256^2 \times 32$ grid points. Although the dense disk is thinner in the model with 0.125 pc resolution, the spiral-like features originated in self-gravitational instability are resolved in both models. Evolution of the mass in the central region ($r \leq 0.75$ pc) is also plotted for the two different resolution. We found that the average mass accretion rate is somewhat larger in the model with smaller resolution (0.125 pc), but the difference is not significant.

If the dense gas disk continues to a larger radius (e.g. $r \sim 100$ pc) with similar surface density, the disk should be highly unstable, therefore larger mass inflow to the central region due to the non-axisymmetric structures or gravity-driven turbulence could be possible. This is an interesting issue to be explored using larger computational box and finer resolution in the near future, as well as the effect of supernova feedback (e.g. Wada & Norman 2002) with the radiative feedback.

TABLE 1
MODEL PARAMETERS AND RESULTANT OBSCURED FRACTION.

Models	M_{BH}^a	γ_{Edd}^b	$L_{AGN,46}^c$	$L_{X,44}^d$	ϕ_i^e	ρ_0^f	$f_{obs,23}^g$	$f_{obs,22}^h$
*7L01	0.13	0.01	0.0016	0.01	0	0.40	0.11	0.33
7L05	0.13	0.05	0.008	0.04	0	0.40	0.14	0.37
7D30	0.13	0.3	0.016	0.18	0	1.22	0.17	0.28
7L20	0.13	0.2	0.032	0.13	0	0.40	0.13	0.24
7D20i	0.13	0.2	0.032	0.13	$\pi/4$	1.22	0.19	0.28
7L30	0.13	0.3	0.048	0.18	0	0.40	0.14	0.22
7D30	0.13	0.3	0.048	0.18	0	1.22	0.22	0.38
7D10	0.13	0.3	0.048	0.07	0	1.22	0.17	0.27
7L40	0.13	0.4	0.064	0.22	0	0.40	0.12	0.68
7D40i	0.13	0.4	0.064	0.22	$\pi/4$	1.22	0.16	0.63
7L40i	0.13	0.4	0.064	0.22	$\pi/4$	0.40	0.12	0.78
8L10	1.3	0.1	0.16	0.45	0	0.40	0.26	0.44
8L20	1.3	0.2	0.32	0.76	0	0.40	0.25	0.45
8D20	1.3	0.2	0.32	0.76	0	1.22	0.21	0.49
8L30	1.3	0.3	0.48	1.03	0	0.40	0.23	0.47
8D30	1.3	0.3	0.48	1.03	0	1.22	0.22	0.50
*8D30i	1.3	0.3	0.48	1.03	$\pi/4$	1.22	0.27	0.95
8L30i	1.3	0.3	0.48	1.03	$\pi/4$	0.40	0.28	0.79
8L40i	1.3	0.4	0.64	1.51	$\pi/4$	0.40	0.43	0.83
*8D50	1.3	0.5	0.8	1.51	0	1.22	0.21	0.66
8D50i	1.3	0.5	0.8	1.51	$\pi/4$	1.22	0.37	0.94
9D10	13	0.1	1.6	2.54	0	1.22	0.31	0.39
*9L40	13	0.4	6.4	7.08	0	0.40	0.25	0.36
9D50	13	0.5	8.0	8.35	0	1.22	0.36	0.48

a : black hole mass ($10^8 M_\odot$), b : Eddington ratio, c : total AGN luminosity (10^{46} erg s $^{-1}$), d : X-ray luminosity (10^{44} erg s $^{-1}$), e : inclination angle of the accretion disk, f : Density of the initial disk ($10^3 M_\odot \text{pc}^{-3}$), g : obscuring fraction for column density ($N_H \geq 10^{23}$ cm $^{-2}$), h : obscuring fraction for column density $N_H \geq 10^{22}$ cm $^{-2}$. Each model name represents “black hole mass” (7, 8, or 9) + density of the initial gas disk (L or D) + Eddington ratio (0.05-0.5) + inclination of the accretion disk (i : $\phi_i = \pi/4$). Models with * in their names are shown in Fig. 1 and 2.

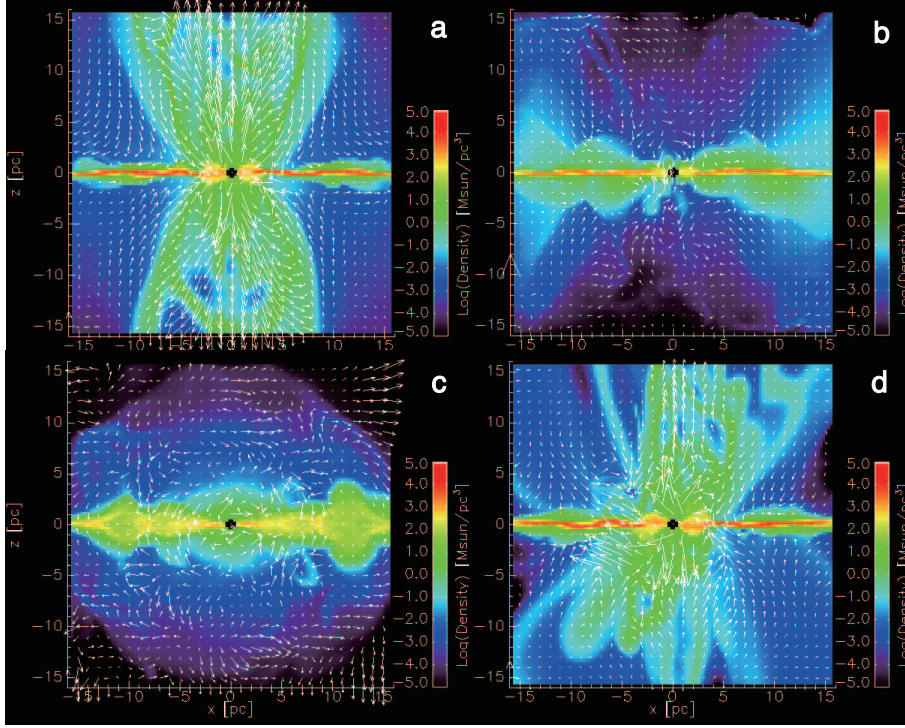


FIG. 1.— (a) Density distribution of the x-z plane for model 8D50 (see Table 1) with the X-ray luminosity $L_{X,44} = 1.51$, black hole mass $M_{BH,8} = 1.3$, Eddington ratio (γ_{Edd}) = 0.5. The central accretion disk inclination $\phi_i = 0$. The bipolar outflows and back flows toward the disk (“radiation-driven fountain”) are formed. (b) Same as (a), but for model 7L01 with $(L_{X,44}, M_{BH,8}, \gamma_{Edd}) = (0.01, 0.13, 0.01)$. No clear outflows are formed. (c) Same as (a), but for model 9L40 with $(L_{X,44}, M_{BH,8}, \gamma_{Edd}) = (7.08, 13.0, 0.4)$. (d) Same as (a), but for model 8D30i with $(L_{X,44}, M_{BH,8}, \gamma_{Edd}) = (1.03, 1.3, 0.3)$, and the central accretion disk is inclined by 45° from the z-axis ($\phi_i = \pi/4$). The arrows represent the relative velocity of the gas on the same plane. (Note that the unit size of the vectors is different for each figure.)

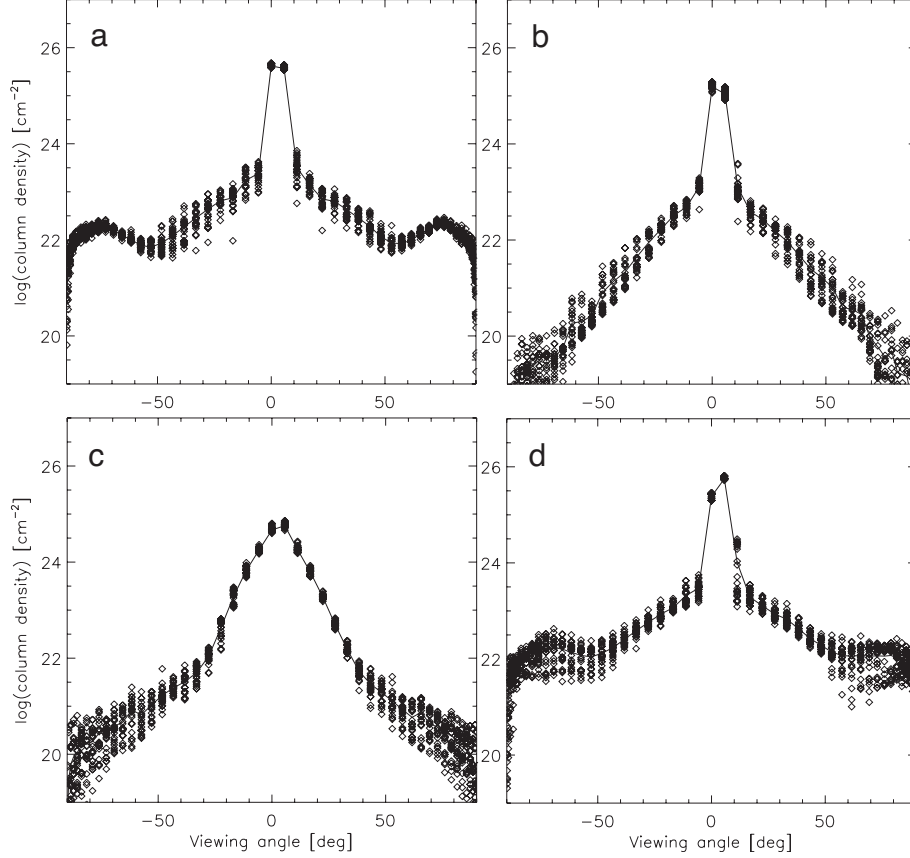


FIG. 2.— Column density distributions toward the nucleus as a function of the viewing angle (0° : edge-on, $\pm 90^\circ$: pole-on) for the same four models shown in Fig. 1 (a: 8D50, b: 7L01, c: 9L40, and d: 8D30i). For a given viewing angle, the dispersion of N_{H} reflects the inhomogeneous density structure of the circumnuclear material. The solid line is the azimuthal average.

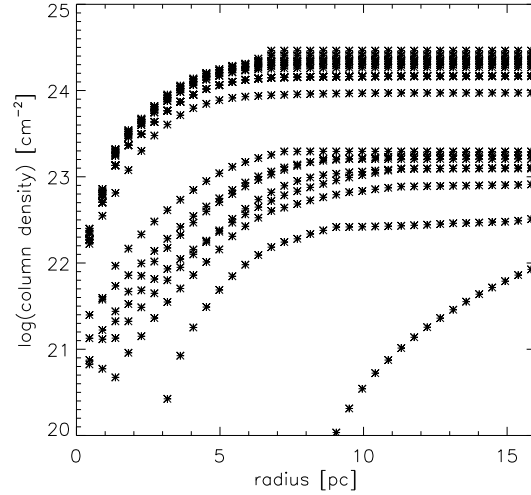


FIG. 3.— Radial distribution of cumulative column densities in model 8D50 (Fig.1a and Fig.2a). The column densities are evaluated along line-of-sights toward the nucleus every about 7 degrees between the rotational axis and the disk plane. It shows that most of the obscuration occurs by the gas inside $r \sim 10$ pc.

REFERENCES

- Aird, J., Coil, A. L., Georgakakis, A., et al. 2015, MNRAS, 451, 1892
 Ballantyne, D. R., Shi, Y., Rieke, G. H., et al. 2006, ApJ, 653, 1070
 Begelman, M. C., McKee, C. F., & Shields, G. A. 1983, ApJ, 271, 70
 Brightman, M., & Nandra, K. 2011, MNRAS, 414, 3084
 Burlon, D., Ajello, M., Greiner, J., et al. 2011, ApJ, 728, 58
 Buchner, J. Georgakakis, A., Nandra, K. et al. ApJ 802, id89 (2015)
 Davies, R., Bartscher, L., Rosario, D., et al. 2015, arXiv:1505.00536

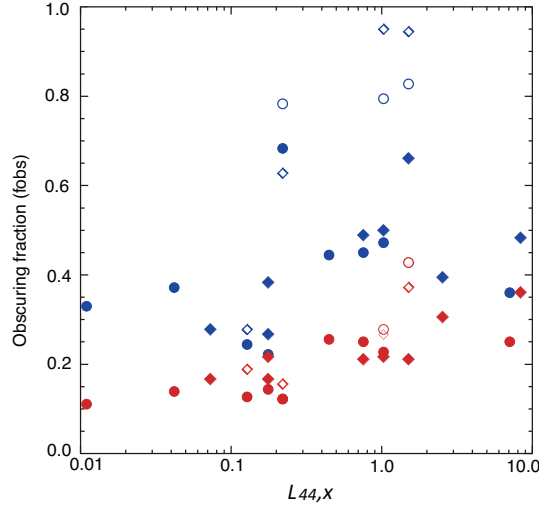


FIG. 4.— Obscuration fraction as a function (f_{obs}) of the X-ray luminosity in 24 models. In each model, f_{obs} is plotted for $N_{22} \equiv 10^{22} \text{ cm}^{-2}$ (blue symbols) and for $N_{23} = 10^{23} \text{ cm}^{-2}$ (red symbols). Circles represent initial gas disks with $\rho_0 = 0.4 \times 10^3 M_{\odot} \text{ pc}^{-3}$, and diamonds represent those with $\rho_0 = 1.22 \times 10^3 M_{\odot} \text{ pc}^{-3}$. Open symbols represent $\phi_i = \pi/4$; that is, the central accretion disk is inclined by 45° (i.e. model names with “i”). See also Fig. 1d and 2d).

- Dorodnitsyn, A., Kallman, T., & Bisnovatyi-Kogan, G. S. 2012, *ApJ*, 747, 8
- Dorodnitsyn, A., Bisnovatyi-Kogan, G. S., & Kallman, T. 2011, *ApJ*, 741, 29
- Elitzur, M. 2006, *New Astronomy Review*, 50, 728
- Elitzur, M., & Shlosman, I. 2006, *ApJ*, 648, L101
- Elvis, M. 2000, *ApJ*, 545, 63
- Elvis, M. 2012, *Journal of Physics Conference Series*, 372, 012032
<http://arxiv.org/abs/1201.5101>
- Enoki, M., Nagashima, M., & Gouda, N. 2003, *PASJ*, 55, 133
- Enoki, M., Ishiyama, T., Kobayashi, M. A. R., & Nagashima, M. 2014, *ApJ*, 794, 69
- Esquej, P., Alonso-Herrero, A., González-Martín, O., et al. 2014, *ApJ*, 780, 86
- Fanidakis, N., Baugh, C. M., Benson, A. J., et al. 2011, *MNRAS*, 410, 53
- Hasinger, G. 2008, *A&A*, 490, 905
- Han, Y., Dai, B., Wang, B., Zhang, F., & Han, Z. 2012, *MNRAS*, 423, 464
- Hopkins, P. F., Richards, G. T., & Hernquist, L. 2007, *ApJ*, 654, 731
- Jia, J., Ptak, A., Heckman, T., & Zakamska, N. L. 2013, *ApJ*, 777, 27
- Kawaguchi, T., & Mori, M. 2010, *ApJ*, 724, L183
- La Franca, F., Fiore, F., Comastri, A., et al. 2005, *ApJ*, 635, 864
- Laor, A., & Draine, B. T. 1993, *ApJ*, 402, 441
- Lawrence, A., & Elvis, M. 1982, *ApJ*, 256, 410
- Lawrence, A. 1991, *MNRAS*, 252, 586
- Lawrence, A., Roseboom, I., Mayo, J., et al. 2013, *arXiv:1303.0219*
- Lawrence, A., & Elvis, M. 2010, *ApJ*, 714, 561
- Levenson, N. A., Weaver, K. A., & Heckman, T. M. 2001, *ApJ*, 550, 230
- Liou, M., Steffen, C., 1993, *J. Comp. Phys.*, 107, 23
- Liou, M., 1996, *J. Comp. Phys.*, 129, 364
- Lusso, E., Hennawi, J. F., Comastri, A., et al. 2013, *ApJ*, 777, 86
- Marconi, A., Risaliti, G., Gilli, R., et al. 2004, *MNRAS*, 351, 169
- Maloney, P. R., Hollenbach, D. J., & Tielens, A. G. G. M. 1996, *ApJ*, 466, 561
- Maiolino, R., Shemmer, O., Imanishi, M., et al. 2007, *A&A*, 468, 979
- Meijerink, R., & Spaans, M. 2005, *A&A*, 436, 397
- Merloni, A., & Heinz, S. 2013, *Planets, Stars and Stellar Systems. Volume 6: ed W. Keel, Extragalactic Astronomy and Cosmology*, p. 503 (arXiv: 1204.4265)
- Merloni, A., Bongiorno, A., Brusa, M., et al. 2014, *MNRAS*, 437, 3550
- Nenkova, M., Sirocky, M. M., Ivezić, Ž., & Elitzur, M. 2008, *ApJ*, 685, 147
- Netzer, H. 1987, *MNRAS*, 225, 55
- Netzer, H. 2015, *ARA&A*, 53, 365 (arXiv:1505.00811)
- Nomura, M., Ohsuga, K., Wada, K., Susa, H., & Misawa, T. 2013, *PASJ*, 65, 40
- Oh, K., Yi, S. K., Schawinski, K., et al. 2015, *ApJS*, 219, 1
- Pâris, I., Petitjean, P., Aubourg, É., et al. 2014, *A&A*, 563, A54
- Pier, E. A., & Krolik, J. H. 1993, *ApJ*, 418, 673
- Proga, D., Stone, J. M., & Kallman, T. R. 2000, *ApJ*, 543, 686
- Roseboom, I. G., Lawrence, A., Elvis, M., et al. 2013, *MNRAS*, 429, 1494
- Shi, J., & Krolik, J. H. 2008, *ApJ*, 679, 1018
- Schartmann, M., Burkert, A., Krause, M., et al. 2010, *MNRAS*, 403, 1801
- Schartmann, M., Wada, K., Prieto, M. A., Burkert, A., & Tristram, K. R. W. 2014, *MNRAS*, 445, 3878
- Shao, L., Kauffmann, G., Li, C., Wang, J., & Heckman, T. M. 2013, *MNRAS*, 436, 3451
- Simpson, C. 2005, *MNRAS*, 360, 565
- Treister, E., Krolik, J. H., & Dullemond, C. 2008, *ApJ*, 679, 140
- Urry, C. M., & Padovani, P. 1995, *PASP*, 107, 803
- Ueda, Y., Akiyama, M., Ohta, K., & Miyaji, T. 2003, *ApJ*, 598, 886
- Ueda, Y., Akiyama, M., Hasinger, G., Miyaji, T., & Watson, M. G. 2014, *ApJ*, 786, 104
- Wada, K. 2001, *ApJ*, 559, L41
- Wada, K. 2012, *ApJ*, 758, 66 (Paper I)
- Wada, K., Meurer, G., & Norman, C. A. 2002, *ApJ*, 577, 197
- Wada, K. & Norman, C. A. 2002, *ApJ*, 566, L21 (WN02)
- Wada, K., Papadopoulos, P. P., & Spaans, M. 2009, *ApJ*, 702, 63
- Wada, K., Meurer, G., & Norman, C. A. 2002, *ApJ*, 577, 197

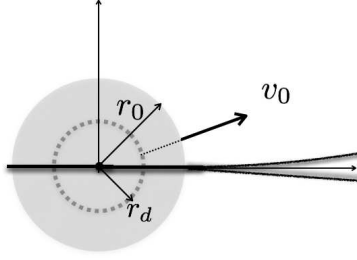


FIG. 5.— Schematic of the radiation-driven outflows, where r_d is the dust sublimation radius, r_0 is the thermal equilibrium radius in terms of the X-ray heating, and v_0 is the velocity of the dusty gas at $r = r_0$. See discussion in §4.

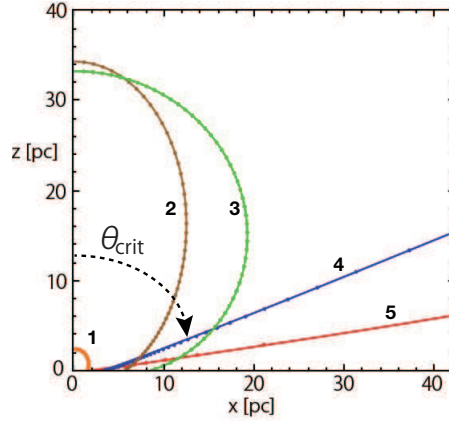


FIG. 6.— The maximum radius of the radiation-accelerated gas $r_{max}(L_{AGN}(\theta), M_{BH})$ (eq. 5) on a $x-z$ plane for five parameter sets: $(L_{46}, M_{BH,8}) = (0.02, 0.1)$, $(0.2, 1.0)$, $(10.0, 10.0)$, $(2.0, 10.0)$, and $(0.01, 1.0)$, with red (denoted by no. 5), blue (4), green (3), brown (2), and orange (1) solid lines, respectively. If r_{max} are finite values for any angles (e.g., no. 1, 2, and 3), the escape velocity of the outflow gas is not large enough, then no steady outflows are expected. On the other hand, if r_{max} becomes infinity for $\theta < \theta_{crit}$, as for no. 4 and 5, we expect bipolar outflows with a half-opening angle of θ_{crit} , and “failed winds” for launched gas with finite r_{max} . For these cases, we suppose that the obscuring fraction f_{obs} is close to $1 - 2\theta_{crit}/\pi$.

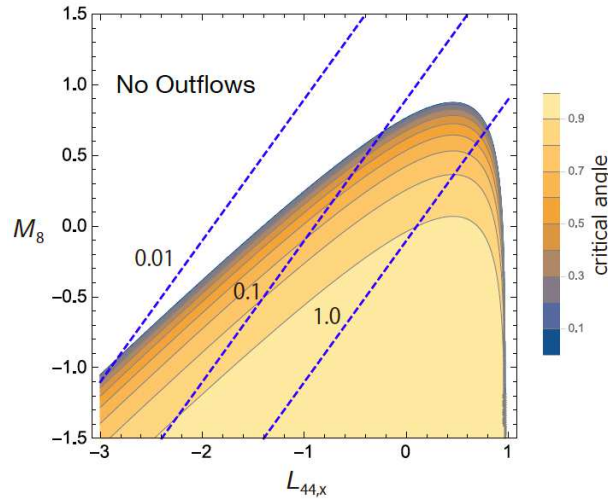


FIG. 7.— The critical angle of the radiation-accelerated gas $\theta_{crit}/(\pi/2)$ (eq. (7)) as a function of the X-ray luminosity $L_{X,44} \equiv L_X/10^{44} \text{ erg s}^{-1}$ and the black hole mass $M_8 \equiv M_{BH}/10^8 M_\odot$. In the colored region, $r_{max}(\theta)$ has a finite value (e.g. models 4 and 5 in Fig. 5), bipolar outflows are expected, and θ_{crit} roughly corresponds the half-opening angle of the outflows. Therefore for a larger θ_{crit} , f_{obs} tends to be smaller. The three dashed lines indicate the Eddington ratios (γ_{Edd}) of 1.0, 0.1, and 0.01. Note that for a given γ_{Edd} , θ_{crit} is not constant, suggesting the obscuring nature is not determined only by γ_{Edd} (see discussion in §4).

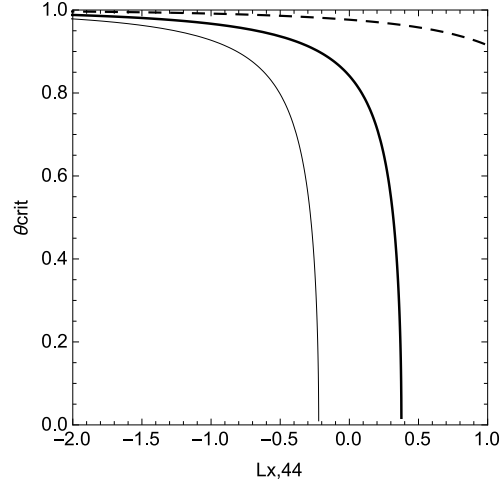


FIG. 8.— Opening angle of the outflows as a function of the X-ray luminosity for three different gas densities $\rho_g (\times 10^2 M_\odot \text{pc}^{-3}) = 1.0$, 5.0, and 10.0 (dashed line, thick solid line, and thin solid lines, respectively), assuming a constant Eddington ratio of 0.2.

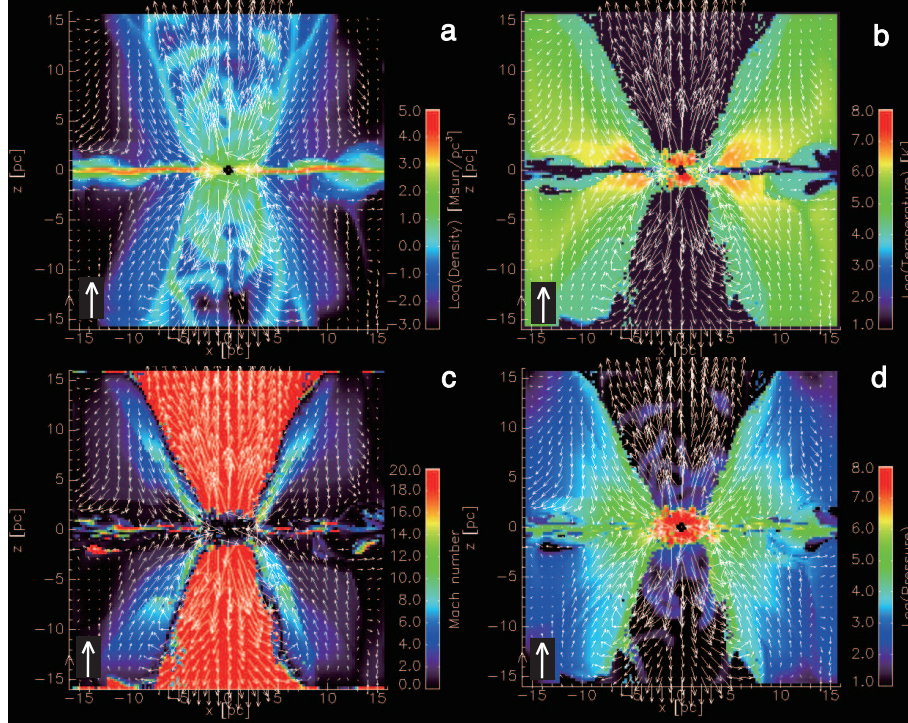


FIG. 9.— (a) density ρ_g , (b) temperature T_g , (c) Mach number for vertical direction, and (d) pressure $\equiv \rho_g T_g$ of model 8D50 at $t = 1.33$ Myr. Vectors are velocities on the x-z plane. A unit vector of 500 km s^{-1} is shown in each panel.

Woods, D. T., Klein, R. I., Castor, J. I., McKee, C. F., & Bell,
J. B. 1996, ApJ, 461, 767

Xu, Y.-D. 2015, MNRAS, 449, 191

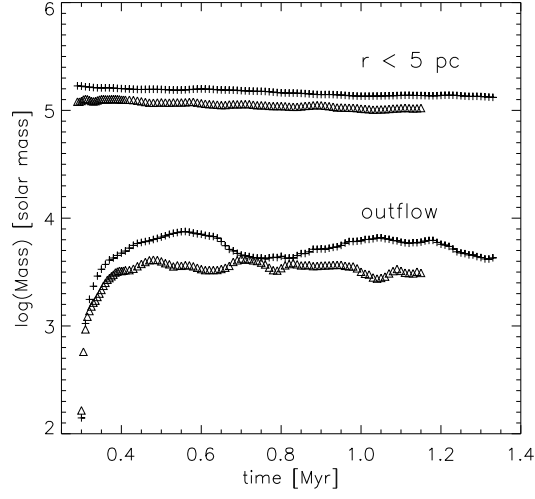


FIG. 10.— Evolution of mass of the outflows ($|z| > 5$ pc) and the core ($r < 5$ pc) in model 8D50 (triangles) and 8D30i (crosses).

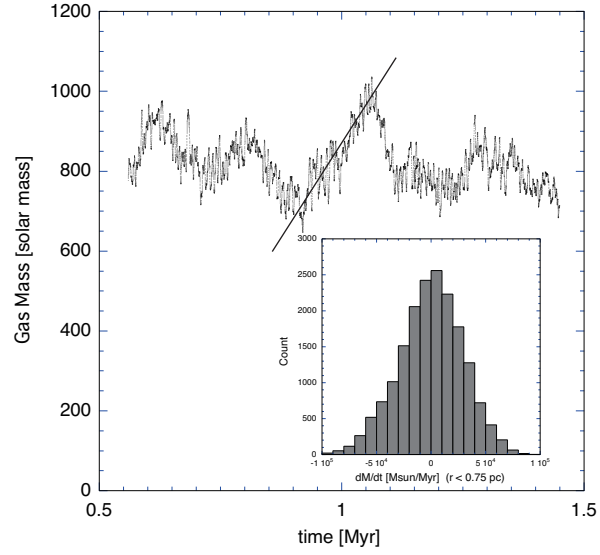


FIG. 11.— Evolution of gas mass inside $r = 0.75$ pc and histogram of dM/dt in model 8iD30i. The root mean square of dM/dt is $0.3 M_{\odot} \text{ yr}^{-1}$. The solid line around $t = 1$ Myr represents the average accretion rate of $2 \times 10^{-3} M_{\odot} \text{ yr}^{-1}$.

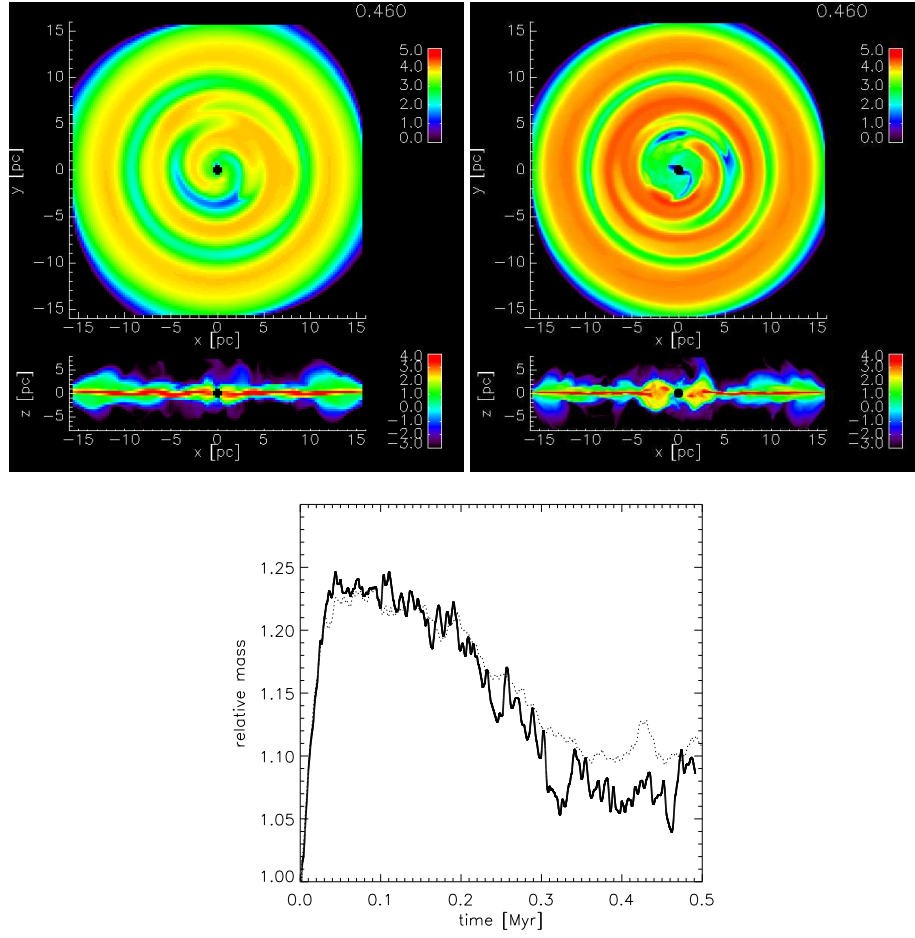


FIG. 12.— Test calculations of a disk without the radiation feedback in order to see effect of the resolution to the mass accretion through the disk. The black hole mass is $1.3 \times 10^7 M_\odot$ and the initial density of the disk is $1.22 \times 10^3 M_\odot \text{ pc}^{-3}$. (left) density for the model with 0.25 pc resolution at $t = 0.46$ Myr (right) Same as the left panel, but with 0.125 pc resolution. The color bar is log-scaled volume density ($M_\odot \text{ pc}^{-3}$). (bottom) Evolution of the mass normalized to the initial value near the inner boundary ($r \leq 0.75$ pc). Thick and dotted lines are the runs with 0.125 pc and 0.25 pc resolution, respectively.